AIAA JOURNAL
Vol. 44, No. 4, April 2006

Study of Wetting in an Asymmetrical Vane–Wall Gap in Propellant Tanks

Yongkang Chen* and Steven H. Collicott†
Purdue University, West Lafayette, Indiana 47907-2023

Wetting of an asymmetrical vane–wall gap geometry is investigated. The geometry is common in vane-type liquid propellant management devices. Critical wetting conditions are determined by applying the method by Concus and Finn (Concus, P., and Finn, R., "On Capillary Free Surfaces in the Absence of Gravity," *Acta Mathematica*, Vol. 132, 1974, pp. 177–198). The critical wetting condition is expressed in terms of critical contact angle as a function of gap size, with the vane thickness and obliquity angle as relevant parameters. It is found that the increase of both the vane thickness and the obliquity angle improves the critical wetting conditions. The analytical results are confirmed with Surface Evolver numerical computations, which also provide graphical descriptions of capillary surfaces. Results from drop tower experiments confirm the analysis and also reveal that the advance rate of the meniscus tip decreases with the gap size when other parameters are fixed.

Nomenclature

L	=	meniscus tip location, mm
R_0	=	radius of arc Γ_0 of C-singular solution
R_γ	=	radius of arc Γ
$\tilde{r}$	=	inner radius of the test cell, mm
t	=	time, s
α	=	vane obliquity angle, deg
Γ	=	name and length of arc Γ
$\Gamma_{\rm cr}$	=	name and length of critical arc Γ
Γ_0	=	name and length of arc Γ of C-singular solution
γ	=	contact angle, deg
$\gamma_{\rm cr}$	=	critical contact angle, deg
δ, $\tilde{\delta}$	=	dimensionless, dimensional, mm, gap size
$\delta_{\rm cr}$	=	critical gap size
ϵ, $\tilde{\epsilon}$	=	dimensionless, dimensional, mm, vane thickness
θ	=	one-half of angle spanned by arc Γ
Σ	=	perimeter of Ω
Σ^*, Σ_0	=	name and length of subarcs of Σ
Φ	=	functional in method by Concus and Finn[3]
Ω	=	name and area of problem domain
Ω^*, Ω_0	=	name and area of subdomain of Ω

Introduction

PERFORMANCE of vane-type propellant management devices (PMD) in weightlessness is vital to positioning, controlling, and transporting the liquid propellant in fuel tanks for successful operation of spacecraft. Proper performance, such as reorienting the propellant following a maneuver, is enabled by a critical contact angle condition. For contact angles below this critical value, a finite height single-valued capillary surface fails to exist in a cylindrical container.[1] As a result, a capillary-driven flow will ensue that is important to successful PMD operation. Similarly, for a given contact angle, a gap between the vane and the wall must be sufficiently small to create the necessary wicking flows.

In a previous study,[2] critical wetting conditions have been determined for the symmetric configurations in which the vane is perpendicular to the tank wall, thus, with $\alpha = 0$, in Fig. 1. Figure 1 shows a comparison of the menisci in a corner and in the vane–wall gap geometry. The reason for making such a comparison is that the existence of the gap can substantially change the properties related to capillarity, as presented by Chen and Collicott.[2] The critical wetting conditions are determined by applying the method by Concus and Finn (see Ref. 2 and references therein for more details). There are several geometric parameters involved in the problem such as the gap size, the vane thickness, and the contact angle. The effects of these parameters have been examined by allowing only one parameter to vary at a time. The results were presented in the form of the critical contact angle or the critical gap size.

Most spacecraft PMD vanes are flexible and likely never perfectly perpendicular to the wall, and, therefore, the symmetric configuration is only an ideal condition. Thus, it is important to study asymmetric configurations in which the vane is not perpendicular to the tank wall to determine how a tilt of the vane affects the wicking power of the geometry. Consequently, there is an extra geometric parameter compared to the symmetric configuration, that is, the vane obliquity angle α as shown in Fig. 1. In the following text, the effects of the relevant geometric parameters on the critical wetting conditions are determined. This is followed by Surface Evolver computations to determine the critical contact angle to confirm the analysis and to provide graphic descriptions of the capillary surfaces. In the end, results from drop-tower experiments that confirm the analysis and show the wicking rates are reported.

Analysis

The foundations for the analysis are described by several authors.[3,4] The notation and methodology from Concus and Finn[3] are followed in this paper. Consider a cross section of a cylindrical container with its bottom completely covered with liquid, as shown in Fig. 2. Ω denotes the entire domain and Σ denotes the boundary of Ω. The domain Ω of type 1 has an interior corner, whereas in the type 2 domain a reentrant corner Λ exists on the boundary of Ω with an angle greater than 180 deg measured from inside Ω.

Assume that the free surface intersects the cross section along an arbitrary circular arc Γ of radius R_γ given by

$$R_\gamma = \Omega/\Sigma \cos\gamma \tag{1}$$

Γ must meet the boundary wall at the contact angle γ. (There are two such arcs in the type 2 domain of Fig. 2.) In the presence of a reentrant corner Λ, the angle at which Γ meets the edge of the

Presented as Paper 2003-4893 at the AIAA/ASME/SAE/ASEE 39th Joint Propulsion Conference, Huntsville, AL, 20–23 July 2003; received 24 January 2005; revision received 27 October 2005; accepted for publication 3 November 2005.

*Postdoctoral Fellow, School of Aeronautics and Astronautics; currently Postdoctoral Fellow, P.O. Box 751-ME, Mechanical and Materials Engineering Department, Portland State University, Portland, OR 97207-0751. Member AIAA.

†Associate Professor, School of Aeronautics and Astronautics. Associate Fellow AIAA.

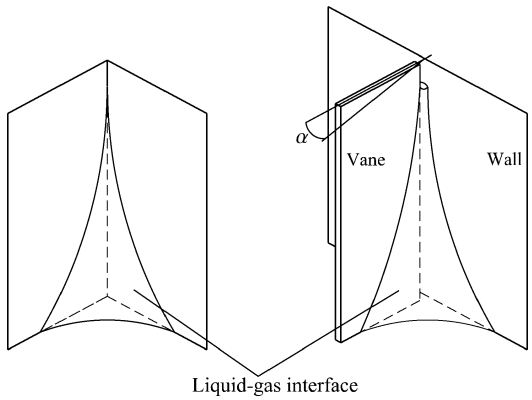

Fig. 1 Capillary menisci in solid interior corner (left) and vane–wall junction with gap (right); α is angle formed between vane plane and normal of wall.

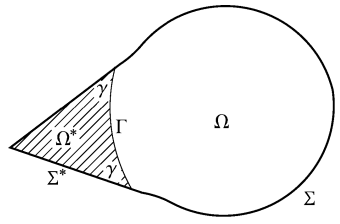

a) Type 1

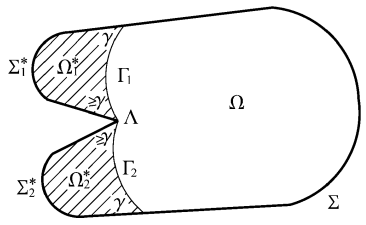

b) Type 2

Fig. 2 General domain Ω and $\{\Gamma;\gamma\}$ configurations.

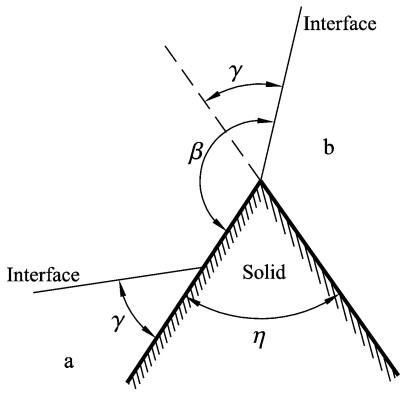

Fig. 3 Demonstration of Gibbs's inequality: γ is equilibrium contact angle and η is corner angle at solid edge; one extreme location, at which $\beta = \pi - \eta + \gamma$, for interface meeting the solid edge is shown.

corner is dictated by Gibbs's inequality,

$$\gamma \le \beta \le \pi - \eta + \gamma \tag{2}$$

where γ is the equilibrium contact angle, β is the angle at which the free surface meets the edge of the corner measured within fluid labeled with an a, and η is the angle of the corner at the edge (measured in the solid part), as shown in Fig. 3. A rigorous description of Gibbs's inequality can be found in Ref. 5.

The arc Γ and subarc $\Sigma^* \subset \Sigma$ bound a subdomain $\Omega^* \subset \Omega$ (Fig. 2). A functional defined as

$$\Phi(\Gamma) = \Gamma - (\cos\gamma)\Sigma^* + (\Sigma\cos\gamma/\Omega)\Omega^* \tag{3}$$

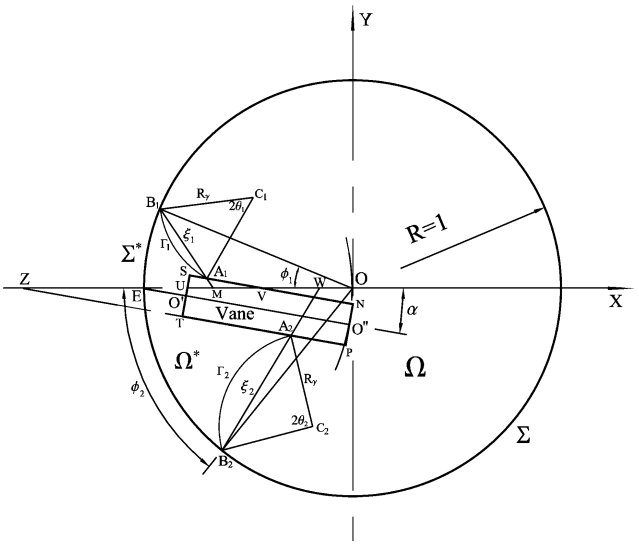

Fig. 4 Problem domain and $\{\Gamma;\gamma\}$ configuration: Σ^* consists of arcs B_1E and B_2E; Ω^* is bounded by Σ^*, Γ_1, and Γ_2 and part of vane surface including A_1S, ST, and TA_2.

is to be evaluated on Ω^*. Subsequently, the existence of a single-valued finite height equilibrium capillary surface can be determined by evaluating the value of Φ for every admissible Γ.

More specifically, for every such arc Γ, if $\Phi > 0$, there is always a single-valued finite height equilibrium surface covering the bottom of the cylinder in zero gravity. In other words, the free surface extends to a finite height at every point in Ω (inside the cylinder). When, for a certain combination of parameters described hereafter, there is a Γ that makes $\Phi \le 0$, then no single-valued finite height equilibrium surface will exist, or, in other words, the free surface extends to infinite height in a subdomain that $\supseteq \Omega^*$ that has higher curvature on its boundary among the whole domain Ω, provided that there is sufficient liquid to cover the base of the cylinder. The contact angle at which $\Phi = 0$ is called the critical contact angle, denoted as γ_{cr}, and the corresponding Γ is called critical arc, denoted as Γ_{cr}. Similarly, for a given contact angle, the gap size at which $\Phi = 0$ is called the critical gap size, denoted as δ_{cr}. Normally, there are at most a finite number of Γ that can be drawn for each geometric configuration, and, therefore, it is necessary to evaluate Φ for only a small number of cases.

The cross-section geometry is shown in Fig. 4. Rectangle *STPN* represents the cross section of the vane. The gap formed between the side *ST* and the cylinder wall is nonuniform. A nominal gap size, denoted as δ, is defined as the distance EO', where O' is the center point of *ST*. *ST* intersects the x axis at point U, whereas the sides *NS* and *PT* intersect the x axis at V and Z, respectively. The obliquity angle α of the vane is defined as the angle between EO and EO' because EO' is always parallel to the long sides of the vane cross section. The gap size δ is varied by changing EO' while the other end of the vane PN remains stationary. Note that $EO'' = R = 1$, where O'' is the center of side PN.

As for different α, formulas for calculating Ω^* and Σ^* might be different. As an example, those formulas with a y coordinate of corner S, thus, $y_S \ge 0$ (formulas for $y_S < 0$ are presented in the Appendix), are presented hereafter as

$$\Omega = \pi - (1-\delta)\epsilon \tag{4}$$

$$\Omega^* = \Omega_1^* + \Omega_2^* \tag{5}$$

$$\Omega_1^* = 0.5\phi_1 - 0.5\lambda\sin\phi_1 - \left(R_\gamma^2\theta_1 - 0.5\xi_1 R_\gamma\cos\theta_1\right) - \Delta_1 \tag{6}$$

$$\Omega_2^* = 0.5\phi_2 - 0.5\rho\sin\phi_2 - \left(R_\gamma^2\theta_2 - 0.5\xi_2 R_\gamma\cos\theta_2\right) - \Delta_2 \tag{7}$$

$$\Sigma = 2\pi + 2(1-\delta) + 2\epsilon \tag{8}$$

$$\Sigma^* = \phi_1 + \phi_2 + \epsilon + \iota_1 + \iota_2 \tag{9}$$

where

$$\lambda = |x_M|, \qquad \rho = |x_W|$$

$$\xi_1 = A_1B_1 = \sqrt{\left(x_{B_1} - x_{A_1}\right)^2 + \left(y_{B_1} - y_{A_1}\right)^2}$$

$$\xi_2 = A_2B_2 = \sqrt{\left(x_{B_2} - x_{A_2}\right)^2 + \left(y_{B_2} - y_{A_2}\right)^2}$$

$$\phi_1 = \arctan\left(\left|y_{B_1}/x_{B_1}\right|\right), \qquad \phi_2 = \arctan\left(\left|y_{B_2}/x_{B_2}\right|\right)$$

$$\theta_1 = \arcsin(\xi_1/2R_\gamma), \qquad \theta_2 = \arcsin(\xi_2/2R_\gamma)$$

$$\Delta_1 = \left[(x_V - x_U)y_S - (x_V - x_M)y_{A_1}\right]/2$$

$$\Delta_2 = \left[(x_W - x_Z)\left|y_{A_2}\right| - (x_U - x_Z)|y_T|\right]/2$$

$$\iota_1 = A_1S = \sqrt{\left(x_S - x_{A_1}\right)^2 + \left(y_S - y_{A_1}\right)^2}$$

$$\iota_2 = A_2T = \sqrt{\left(x_T - x_{A_2}\right)^2 + \left(y_T - y_{A_2}\right)^2}$$

Γ_1 is the arc on the side where the angle formed between the vane and the cylinder wall is obtuse, whereas Γ_2 is on the side where the angle is acute. Arcs Γ_1 and Γ_2 meet the vane and the cylinder surfaces at A_1, A_2 and B_1, B_2, respectively. Here, ϕ_1 and ϕ_2 are angles spanned by arcs B_1E and B_2E, respectively.

Similar to the configurations where the vane is normal to the container wall, there are two possible locations of Γ as described by Chen and Collicott.[2] Γ of type 1 meets both the tank wall and the vane surface at the contact angle γ, whereas Γ of type 2 meets one edge of the vane at one side and meets the tank wall on the other side, as is discussed hereafter. Note that the four corners at the edges of the vane are reentrant corners in the problem domain Ω as described earlier.

It is then found that there are three combinations of Γ on both sides of the vane. Figures 5–7 give examples for each type of combination. In the first combination, both $(\Gamma_{cr})_1$ and $(\Gamma_{cr})_2$ are type 1 arcs. In the second combination, $(\Gamma_{cr})_1$ is a type 2 arc, whereas $(\Gamma_{cr})_2$ is still a type 1 arc. In the third combination, both $(\Gamma_{cr})_1$ and $(\Gamma_{cr})_2$ are type 2 arcs.

Note that γ_{cr} was first identified for different gap sizes δ and vane thicknesses ϵ with $\alpha = 10$ deg as shown in Fig. 8. Here, ϵ only ranges from 0 to 0.2. Each data line divides the first quadrant into

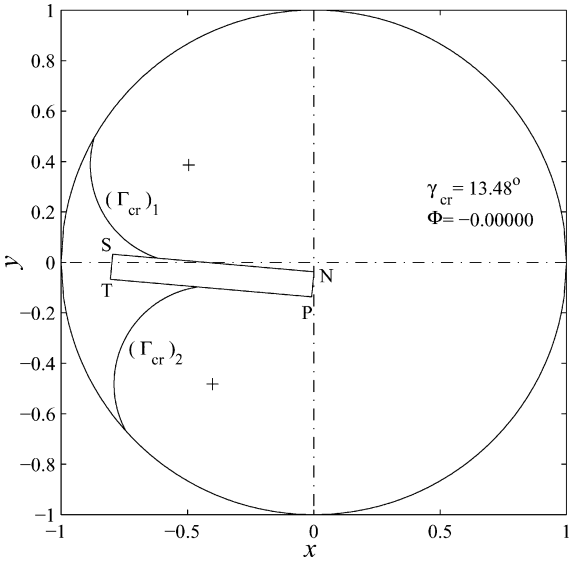

Fig. 5 First combination of arc Γ locations: $\epsilon = 0.1$; $\delta = 0.2$; $\alpha = 5$ deg; and +, center of Γ_{cr}.

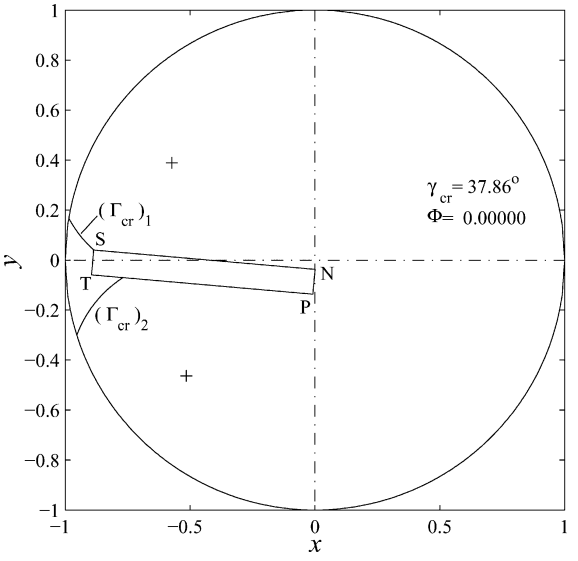

Fig. 6 Second combination of arc Γ locations: $\epsilon = 0.1$, $\delta = 0.11$, and $\alpha = 5$ deg.

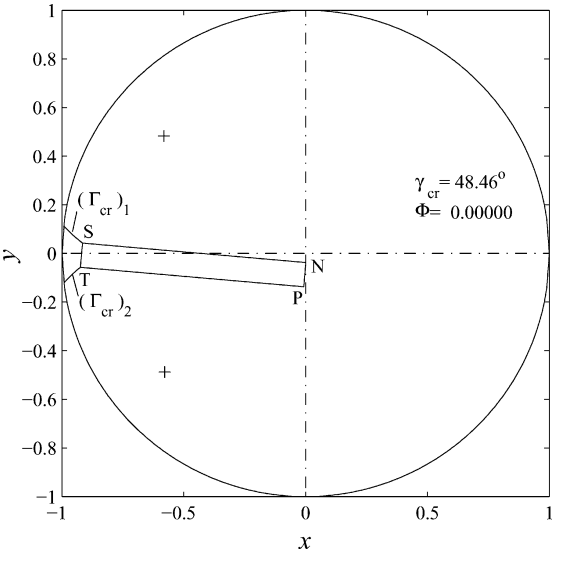

Fig. 7 Third combination of arc Γ locations: $\epsilon = 0.1$, $\delta = 0.08$, and $\alpha = 5$ deg.

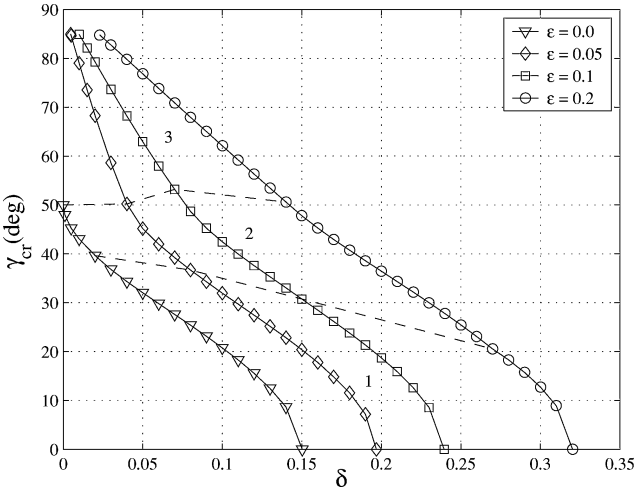

Fig. 8 Critical contact angles for different vane thicknesses at $\alpha = 10$ deg.

two parts. Single-valued finite height equilibrium surfaces exist in the part above the data line, whereas for the part on and below it, single-valued finite height equilibrium surfaces fail to exist. When ϵ is fixed, γ_{cr} decreases with δ. However, when δ is fixed, γ_{cr} increases with ϵ. Each data line can also be divided into three sections as shown in Fig. 8, based on the three combinations of the arcs Γ just described. Thus, section 1 corresponds to the first combination, and so on. The relation between γ_{cr} and δ appears to be nearly linear in section 3. In addition, the lower limit of the gap size for each line is the value at which the finite thickness vane touches the tank wall.

The data in Fig. 8 show the effects of geometric parameters ϵ and δ on γ_{cr} for fixed α. One can also find critical gap size values δ_{cr} for different γ and ϵ from Fig. 8. Specifically, δ_{cr} for given ϵ and γ can be found at the intersection of a horizontal line and the respective data line. This is because γ_{cr} is determined by looking for the arc Γ that makes $\Phi = 0$ for certain ϵ and δ. At $\Phi = 0$, any one of the parameters has the critical value when the others are fixed.

Note also in Fig. 8 that, for every δ, there is somewhat larger increase in γ_{cr} for ϵ changing from 0.1 to 0.2, as compared to those data for smaller ϵ. This is caused by a typical feature for the case $\epsilon = 0.2$; thus, an arc Γ becomes admissible that begins from the lower-right edge of the vane, vertex P in Fig. 4, and meets the cylinder wall at angle γ. Again, the corner at P is a reentrant corner in Ω. Consequently, one can find a Γ_{cr} starting from P that makes $\Phi = 0$ for a larger δ than that for other combinations of arcs Γ at smaller ϵ. This variation is demonstrated in Figs. 9 and 10. The geometry in Fig. 9 where $\epsilon = 0.1$ and $(\Gamma_{cr})_2$ is of type 1, whereas that in Fig. 10 where $\epsilon = 0.2$ and $(\Gamma_{cr})_2$ is of type 2.

When ϵ is fixed at 0.1, γ_{cr} is also determined for different δ and α, which ranges from 0 to 15 deg. The results are shown in Fig. 11. Note that, for $\delta < 0.08$, the angle α has no apparent effect on γ_{cr} and the relation between γ_{cr} and δ appears to be nearly linear. Other than that, γ_{cr} increases with α for a fixed δ. Again, from these results, a critical gap size δ_{cr} can be determined when all of the other parameters including the contact angle are fixed. Similarly, α has no apparent effect on δ_{cr} when $\gamma > 50$ deg and δ_{cr} increases with α otherwise.

The dramatic increase of γ_{cr} (or δ_{cr}) observed when α increases from 10 to 15 deg is caused by $(\Gamma_{cr})_2$ changing from type 1 to 2 as discussed earlier. As an example, locations of Γ_{cr} for $\alpha = 15$ deg at $\gamma = 0$ deg are shown in Fig. 12 and can be compared to those shown in Fig. 9.

Finn and Neel[6] point out that for every $\gamma \leq \gamma_{cr}$, where Φ is nonpositive, there exists at least one solution in a singular sense called the C-singular solution. The technique for identifying such solutions in polygonal cross-section cylinders is described by de Lazzer et al.[7]

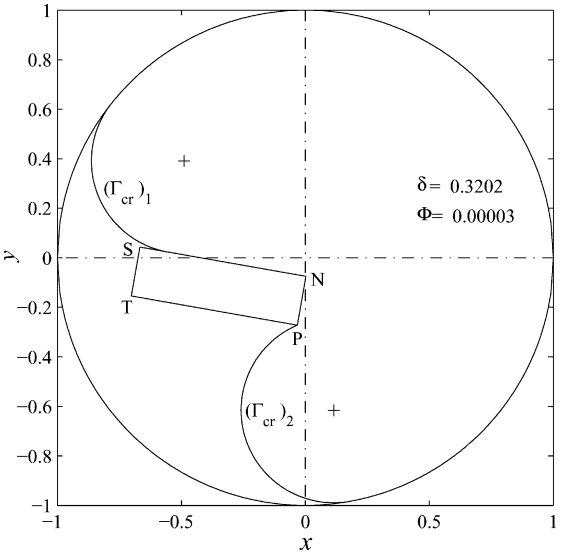

Fig. 10 Critical arc Γ_{cr} location for $\epsilon = 0.2$, $\gamma = 0$ deg, and $\alpha = 10$ deg.

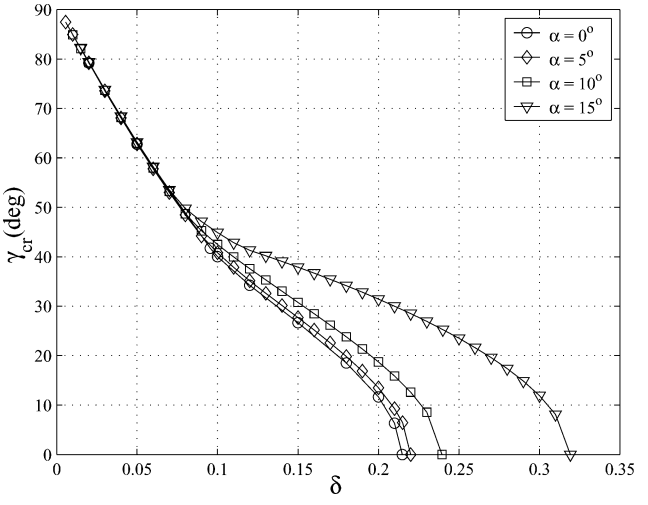

Fig. 11 Critical contact angles for different α at $\epsilon = 0.1$.

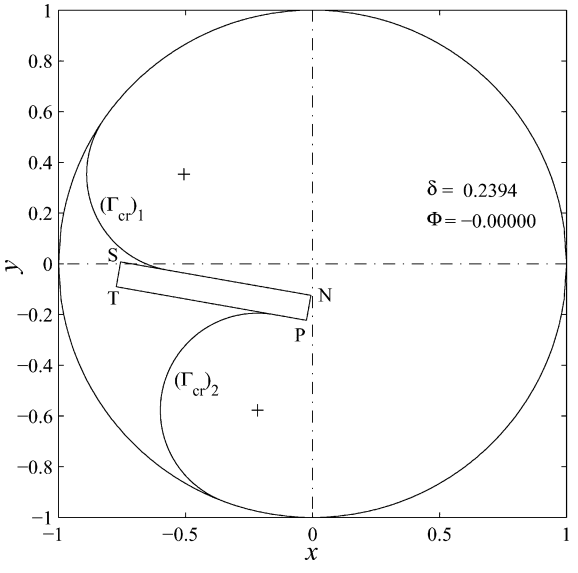

Fig. 9 Critical arc Γ_{cr} location for $\epsilon = 0.1$, $\gamma = 0$ deg, and $\alpha = 10$ deg.

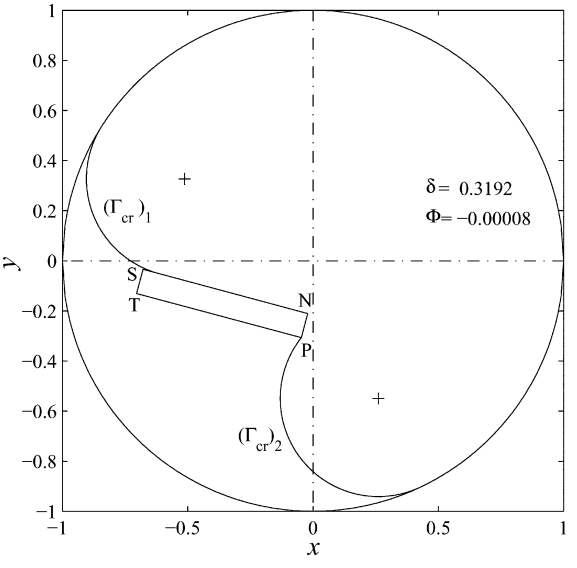

Fig. 12 Critical arc Γ_{cr} location for $\epsilon = 0.1$, $\gamma = 0$ deg, and $\alpha = 15$ deg.

A C-singular solution means that there exists a finite number of arcs Γ_0 of common radius $R_0 \geq R_\gamma$ that bound a subdomain $\Omega_0 \subset \Omega$ with subarcs $\Sigma_0 \subset \Sigma$. Note that Ω_0 is on the concave side of Γ_0 and opposite to Ω^* in Fig. 2. A solution surface is determined up to an additive constant, or, in other words, the capillary surface meets Σ_0 at γ and it approaches Γ_0 asymptotically and extends up to infinite height. Although it appears in the context of studying the equilibrium surfaces, the knowledge of the arc Γ_0 is essential to studying the dynamics of capillary-driven flow in this and other similar geometries.[8,9]

Without going into detail, R_0 can be determined by applying the divergence theorem to the Young–Laplace equation

$$\operatorname{div} \boldsymbol{T}u = 1/R_0 \qquad \text{with} \qquad \boldsymbol{T}u = \nabla u \Big/ \sqrt{1 + |\nabla u|^2} \tag{10}$$

and corresponding boundary conditions over the subdomain Ω_0. This procedure gives rise to

$$\Gamma_0 + \cos\gamma(\Sigma_0) - (\Omega_0)/R_0 = 0 \tag{11}$$

from which R_0 can be determined.

The arc Γ_0 is the same as Γ_{cr} when $\gamma = \gamma_{\text{cr}}$ as one may already notice in Figs. 5–7. For $\gamma < \gamma_{\text{cr}}$, Γ_0 has to be determined separately. Note for Γ_0 that, for a fixed $\gamma < \gamma_{\text{cr}}$, it does not vary with the gap size when the other geometric parameters are fixed.

Surface Evolver Computation

The analysis just conducted and described provides critical wetting conditions for the geometry under investigation. It, however, cannot provide information about the geometric features of the capillary surfaces, be they equilibrium or not. As in Ref. 2, numerical computations using Surface Evolver[10] as a complementary approach can provide a solution for the interface surfaces and can also determine the critical wetting conditions to confirm the analytical results, which in turn will validate Surface Evolver as an important tool in studies where the analytical method is not applicable. Over the past decade, the use of Surface Evolver in studying capillary surfaces has been greatly expanded, and most recent examples can be found in Refs. 11 and 12.

The geometry in the computation is a cylindrical container with a cross section as shown in Fig. 4. In zero gravity, the energy minimized by Surface Evolver includes only the interfacial energies. There are two solid boundaries: the circular cylinder wall and the flat walls of the vane. A detailed formulation of the interface energies can be found in Ref. 13 or examples given by Brakke.[10] For each case computed, the iteration of Surface Evolver starts with a coarse grid of nominally 256 (2^8) facets. With necessary refinement, the number of facets increases to up to approximately 4096 (2^{12}); however, more facets can be produced due to the increase of the interface area as found for γ near and below γ_{cr}.

Three typical cases are computed with the parameters listed in Table 1. In these cases, the effects of the gap size δ are examined with both the vane thickness ϵ and the vane obliquity angle α fixed. The choice of these cases is based on three combinations of two types of the arc Γ that characterize the determination of γ_{cr}.

First, the critical contact angles for these cases are identified as listed in Table 1. Note that the critical values predicted by Surface Evolver are lower than the corresponding analytical results with a maximum error of 3.4%. The discretization of the free surface causes the error, and grid density affects the magnitude of the error. Better accuracy requires more facets, which makes the evolution of the interface extremely slow for contact angles close to or at the analytical critical value. More computer power and computing time is needed to reduce the error. For cases with supercritical parameters, the meniscus tip height is plotted against γ in Fig. 13, in which the critical contact angles identified are marked by the dashed lines. The meniscus tip height increases with the contact angle decreasing from 90 deg. It starts to increase dramatically when the contact angle is close to the critical value because the slope of the data lines increases significantly. Note that in the range of γ, wherever a comparison is possible, the meniscus tip of the configuration with greater γ_{cr} is higher than that of the configuration with smaller γ_{cr}.

Table 1 Cases tested with Surface Evolver

Case	α, deg	ϵ	δ	Analytical γ_{cr}, deg	Surface Evolver γ_{cr}, deg
1	10	0.1	0.18	23.81	23
2	10	0.1	0.12	37.60	37
3	10	0.1	0.06	57.95	57.5

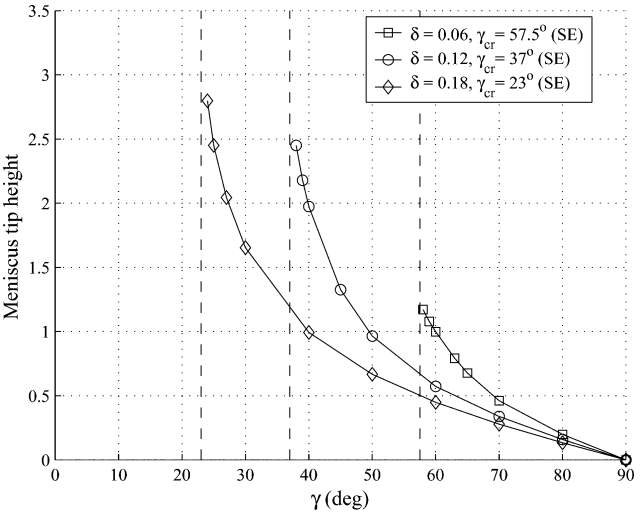

Fig. 13 Equilibrium meniscus tip height at different γ: $\epsilon = 0.1$ and $\alpha = 10$ deg.

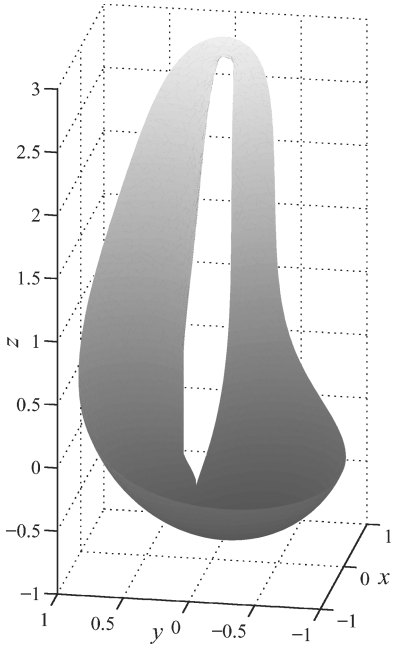

Fig. 14 Equilibrium surface: $\epsilon = 0.1$, $\delta = 0.18$, $\gamma = 24$ deg, and $\alpha = 10$ deg.

For each case, the equilibrium surfaces at supercritical contact angles and the unconverged surfaces at subcritical contact angles are shown in Figs. 14–19. The vane surfaces are not displayed in Figs. 14–19. The unconverged surface is so called because a converged equilibrium surface does not exist. However, the surface provides a graphical description of the configurations where the liquid wicks toward infinity. These unconverged surfaces reveal a typical feature of the C-singular solution surfaces described earlier. Note from Figs. 14–19 that there are vertical liquid columns on the two sides of the vane around the gap as the meniscus tip advances to a great height.

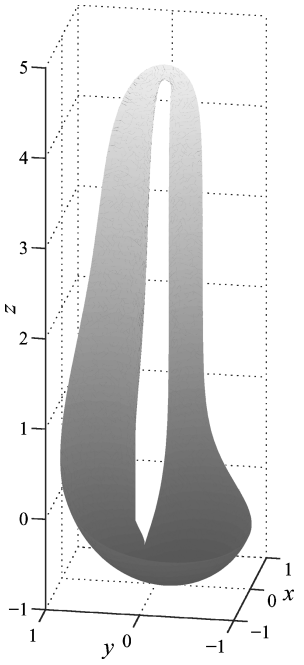

Fig. 15 Unconverged surface: $\epsilon = 0.1$, $\delta = 0.18$, $\gamma = 22$ deg, and $\alpha = 10$ deg.

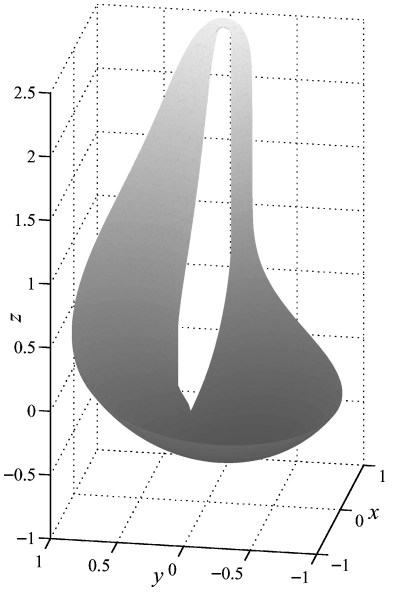

Fig. 16 Equilibrium surface: $\epsilon = 0.1$, $\delta = 0.12$, $\gamma = 38$ deg, and $\alpha = 10$ deg.

The unconverged surfaces for the first case are featured by the first combination of arc Γ (Fig. 5), that is, both arcs are of type 1. The angle formed between the vane and the tank wall is acute on the left-hand side and obtuse on the right-hand side. Apparently, for the unconverged surface, the cross-sectional area of the vertical liquid column on the left-hand side is larger than that of the right-hand side (Fig. 15).

The gap size of the second case is smaller compared to that of the first case. The unconverged surfaces are featured by the second combination of the arc Γ (Fig. 6). Thus, the arc Γ is still of type 1 on the left-hand side, whereas it is of type 2 on the right-hand side. Accordingly, the vertical section of the unconverged surface still meets the vane surface on the left, whereas it retreats to the gap region and attaches to the edge of the vane on the right (Fig. 17).

The unconverged surfaces for the third combination of the arc Γ (Fig. 7), of the last case where the gap is the smallest, is shown in

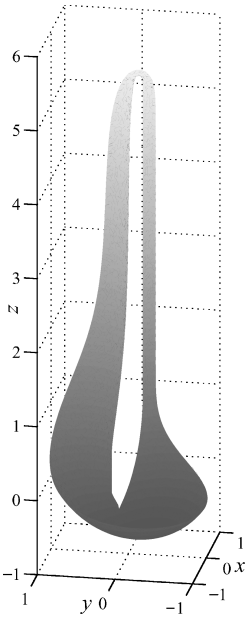

Fig. 17 Unconverged surface: $\epsilon = 0.1$, $\delta = 0.12$, $\gamma = 36$ deg, and $\alpha = 10$ deg.

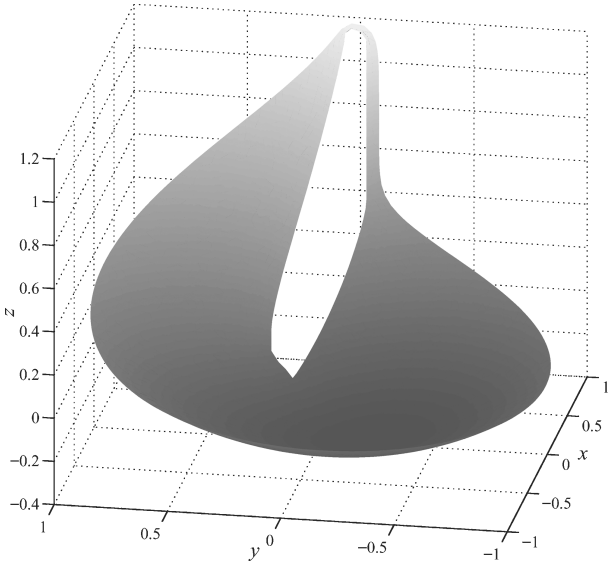

Fig. 18 Equilibrium surface: $\epsilon = 0.1$, $\delta = 0.06$, $\gamma = 58$ deg, and $\alpha = 10$ deg.

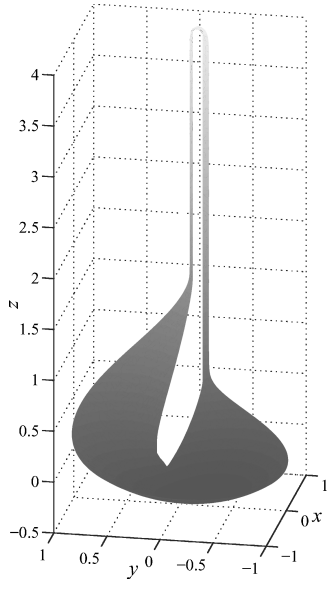

Fig. 19 Unconverged surface: $\epsilon = 0.1$, $\delta = 0.06$, $\gamma = 56$ deg, and $\alpha = 10$ deg.

Fig. 19. Here the arcs Γ on both sides of the vane are of type 2. Thus, the vertical section of the unconverged surface is confined to the gap region, as is visible in Fig. 19.

Drop-Tower Experiment

Experiments were conducted in the drop tower at Purdue University, and a detailed description can be found in Refs. 13 and 14. This facility provides about 1.2 s of free fall in a vacuum. The test cell is shown in Fig. 20. The acrylic cylinder in the center part is the fluid cell with a stainless-steel vane mounted to create a controlled gap between it and the cylinder wall. The test cell is partially filled with 5 cS silicon oil [polydimethylsiloxane (PDMS)], which has close to zero contact angle on both the acrylic and the stainless-steel surfaces. The image data shown hereafter are acquired with a charge-coupled device camera dropping outside of the tower. The framing of the test cell image is affected by the friction and aerodynamic drag forces on the camera system, and it is compensated with a timing scheme.

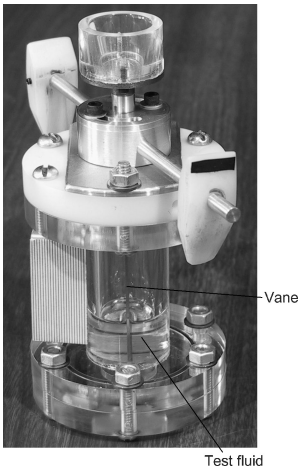

Fig. 20 Test cell partially filled with 5 cSt silicon oil.

In the experiments, the vane thickness, the contact angle, and the vane obliquity angle are fixed, whereas the gap size is varied as listed in Table 2. The largest gap of the four is supercritical according to the analysis and, thus, should yield a single-valued finite height surface. The study reported here is focused on identifying the critical wetting conditions because the study of the dynamics of the capillary flow is reported separately.[15]

A selection of images of menisci during free fall is shown in Fig. 21. The images were taken at the rate of 30 frames per second. Note that all of the images are cropped from the original images. Because of the repeatable shift between the test cell and the camera during each drop, the size of some of cropped images is smaller than others. The images presented here are padded to a uniform size with a constant gray level for this part. Continuous advance of the meniscus tip can be observed for the two small gap values. The advance appears to be slowed after a certain time for the $\tilde{\delta} = 2.54$ mm case. No obvious change of the tip location can be seen after 0.8 s for $\tilde{\delta} = 3.18$ mm.

The time histories of the tip location measured from images such as those in Fig. 21 are shown in Fig. 22. For $\tilde{\delta} = 3.18$ mm, the tip height starts to level off after $t \approx 0.9$ s, as is evident in

Table 2 Parameters of test cell cross-sectional geometry: radius of circular wall $\tilde{r} = 12.7$ mm, $\alpha = 10$ deg, and vane thickness $\tilde{\epsilon} = 1.27$ mm ($\tilde{\epsilon}/\tilde{r} = 0.1$)

Gap size $\tilde{\delta}$, mm	$\tilde{\delta}/\tilde{r}$
0.64	0.05
1.27	0.1
2.54	0.2
3.18	0.25

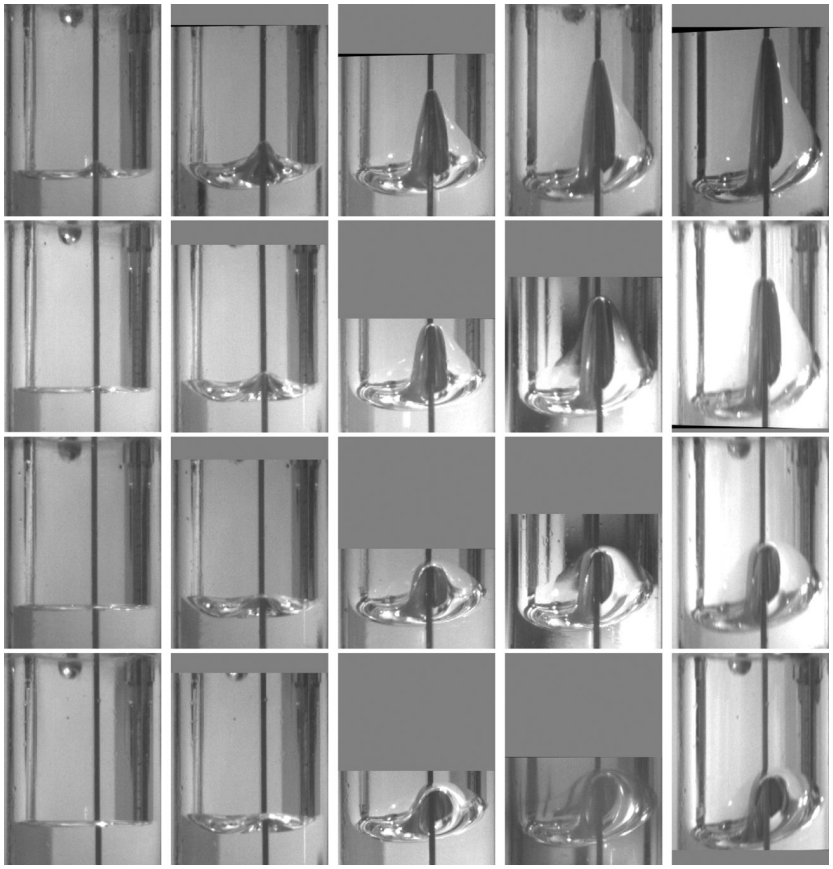

Fig. 21 Meniscus at different moments: 0, 0.1, 0.4, 0.7, 1.0 s left to right; $\tilde{\delta} = 0.64$, 1.27, 2.54, 3.18 mm top to bottom row; $\alpha = 10$ deg; test fluid, 5 cS silicon oil; height of each image indicates 60 mm in reality.

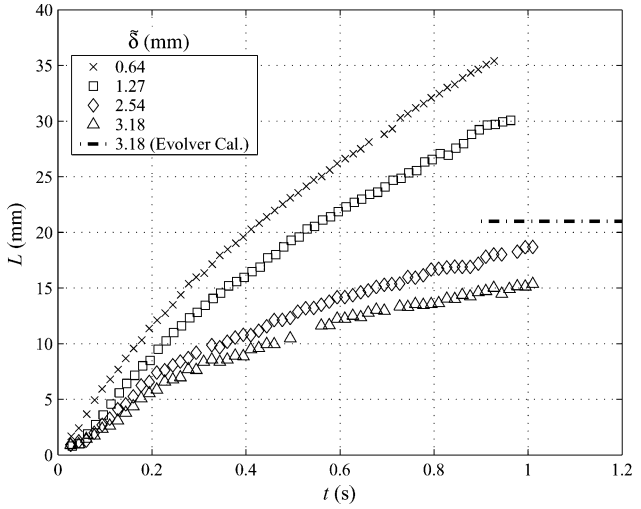

Fig. 22 Time history of meniscus tip location: $\tilde{\epsilon} = 1.27$ mm, $\gamma = 0$ deg, and $\alpha = 10$ deg.

Fig. 22. A continuous increase of the tip height for $\tilde{\delta} = 0.64$ and 1.27 mm throughout the free fall can be noticed. The data of $\tilde{\delta} = 2.54$ mm are inconclusive because the capillary flow becomes extremely slow for the gap smaller than, but close to, the critical value. For the supercritical case, the equilibrium meniscus tip location computed using Surface Evolver is shown by the dash–dot line in Fig. 22. Note that the result is obtained at a 5-deg contact angle because it can be very difficult to determine convergence of the free surface if the contact angle is zero. In spite of this, there is a 28.6% difference between the experiment and the numerical data.

Overall, interfaces of limited height are observed for the supercritical gap size. A continuously advancing meniscus tip is observed for subcritical gaps except for the gap size that is close to the critical value.

There are several sources of error in the experimental study. The first is the determination of the moment when the test cell starts the free fall. The camera starts to capture an image sequence before the free fall starts, and the initial moment of it is determined by identifying the initial variation of the interface in the images captured. Generally, the free fall starts between two successive images. This error is believed to be within 17 ms based on the frame rate of the camera. Fortunately, this error only causes a shift of the whole data set along the time axis without affecting other aspects of the results.

The second source of error involves the shift between the test cell and the camera. It influences the reading of the meniscus tip height. Quantitative analysis shows that the maximum error is around 1.8 mm (Ref. 13).

The last source of error that causes the scattering of the data might be the contact angle hysteresis[16] that tends to halt the advance of the contact line. It is caused by pinning of the contact line due to the heterogeneity of the solid surfaces. This, and the gravity residual during the free fall, account for the difference between the experimental and numerical tip location of the equilibrium surface for the supercritical gap size.

Conclusions

Critical wetting conditions in an asymmetric vane–wall gap geometry are determined by applying the method by Concus and Finn.[3] Effects of relevant parameters within certain ranges including the vane thickness, gap size, the vane obliquity angle, and the contact angle of the fluid are examined. The analytical results are confirmed with numerical computation using Surface Evolver and drop-tower experiments. In addition, graphical descriptions of the capillary surfaces are obtained from the numerical study. The understanding gained in this study about the asymmetrical vane–wall gap is helpful in evaluating the performance and helping in the design of vane-type PMD. Specific conclusions are as follows:

1) The critical wetting conditions are governed by both the gap and the corners formed between the vane and the container wall. There exist three combinations of the locations for the critical arc Γ_{cr} depending on the vane thickness, the gap size, and the vane obliquity angle.

2) In this study, the critical wetting conditions are expressed in terms of a critical contact angle or critical gap size. At a fixed vane obliquity angle α, the critical contact angle (when the gap is fixed) increases with the vane thickness and so does the critical gap size (when the contact angle is fixed). At a fixed vane thickness, the critical contact angle appears not to vary with α when the gap size is smaller than 0.08; otherwise, it increases with α. Similarly, at a fixed contact angle, the critical gap size appears not to vary with α when the contact angle is greater than 50 deg; otherwise, it increases with α.

3) Constrained by computer power and computing time available, numerical computation using Surface Evolver appears to underpredict the critical wetting conditions. The maximum error, however, in determining the critical contact angle among the computed cases is 3.4%. The computations also provide graphical description of the capillary surfaces, typically the features of C-singular solution surfaces.

4) The drop-tower experiments provide data that confirm the analytical result and show that the wicking rate decreases with the gap size.

5) The study of the effects of small angular changes in vane alignment, as expected for thin flexible PMD vanes, shows that this component of a traditional PMD design is tolerant to vane misalignments.

Appendix: Formulas for $y_S < 0$

Figure A1 shows the configuration where $y_S < 0$. Note that Γ_1 and Γ_2 meet the vane and the cylinder wall surfaces at A_1, A_2, and B_1, B_2 respectively. The formulas for calculating Ω^*, Ω, Σ, and Σ^* are

$$\Omega = \pi - (1 - \delta)\epsilon \tag{A1}$$

$$\Omega^* = \Omega_1^* + \Omega_2^* \tag{A2}$$

$$\Omega_1^* = 0.5\phi_1 - 0.5|x_G|y_{B_1} - \left(R_\gamma^2\theta_1 - 0.5\xi_1 R_\gamma \cos\theta_1\right) \tag{A3}$$

$$\Omega_2^* = 0.5\phi_2 - 0.5x_W y_{B_2} - \left(R_\gamma^2\theta_2 - 0.5\xi_2 R_\gamma \cos\theta_2\right) - \sum_{i=1}^{3}\Delta_i \tag{A4}$$

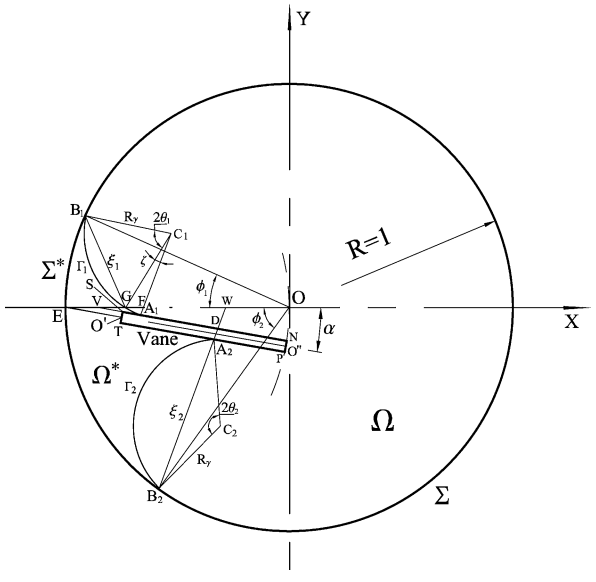

Fig. A1 Problem domain and $\{\Gamma;\gamma\}$ configuration with $y_S < 0$.

$$\Sigma = 2\pi + 2(1-\delta) + 2\epsilon \tag{A5}$$

$$\Sigma^* = \phi_1 + \phi_2 + \epsilon + \iota_1 + \iota_2 \tag{A6}$$

where

$$\xi_1 = GB_1 = \sqrt{\left(x_{B_1} - x_G\right)^2 + \left(y_{B_1} - y_G\right)^2}$$

$$\xi_2 = A_2B_2 = \sqrt{\left(x_{B_2} - x_{A_2}\right)^2 + \left(y_{B_2} - y_{A_2}\right)^2}$$

$$\phi_1 = \arctan\left(\left|y_{B_1}/x_{B_1}\right|\right), \qquad \phi_2 = \arctan\left(\left|y_{B_2}/x_{B_2}\right|\right)$$

$$\theta_1 = \arcsin(\xi_1/2R_\gamma), \qquad \theta_2 = \arcsin(\xi_2/2R_\gamma)$$

$$\Delta_1 = FGA_1 = 0.5R_\gamma^2\zeta - 0.5(x_F - x_G)y_{c_1}$$

$$\Delta_2 = WFA_1D = 0.5\left[(x_W - x_V)|y_D| - (x_F - x_V)\left|y_{A_1}\right|\right]$$

$$\Delta_3 = DSTA_2 = 0.5(\iota_3 + \iota_4)\epsilon$$

$$\iota_1 = A_1S = \sqrt{\left(x_S - x_{A_1}\right)^2 + \left(y_S - y_{A_1}\right)^2}$$

$$\iota_2 = TA_2 = \sqrt{\left(x_T - x_{A_2}\right)^2 + \left(y_T - y_{A_2}\right)^2}$$

$$\iota_3 = DS = \sqrt{(x_S - x_D)^2 + (y_S - y_D)^2}$$

$$\iota_4 = TA_2 = \sqrt{\left(x_{A_2} - x_T\right)^2 + \left(y_{A_2} - y_T\right)^2}$$

$$\zeta = 2\arcsin(GA_1/2R_\gamma)$$

Acknowledgments

A gift from the Lockheed Martin Company, matched by the second author's National Science Foundation Career Award CTS 95-01881 and a Purdue Research Foundation Fellowship for the first author enabled construction of the drop tower. The authors thank R. Finn of Stanford University; P. Concus of the University of California, Berkeley; and G. Smedley of Glaukos Corporation for their very helpful discussions of the analysis. Thanks also go to M. Weislogel of Portland State University for many suggestions and discussions about the drop tower experiment.

References

[1]Finn, R., "Capillary Surface Interfaces," *Notices of the AMS*, Vol. 46, No. 7, 1999, pp. 770–781.

[2]Chen, Y., and Collicott, S. H., "Investigation of the Symmetric Wetting of Vane–Wall Gaps in Propellant Tanks," *AIAA Journal*, Vol. 42, No. 2, 2004, pp. 305–314.

[3]Concus, P., and Finn, R., "On Capillary Free Surfaces in the Absence of Gravity," *Acta Mathematica*, Vol. 132, 1974, pp. 177–198.

[4]Myshkis, A., Babskii, V., Kopachevshii, N., Slobozhanin, L., and Tyuptsov, A., *Low-Gravity Fluid Mechanics*, Springer-Verlag, Berlin, 1987, Chaps. 2 and 3.

[5]Finn, R., *Equilibrium Capillary Surfaces*, Vol. 284, Series of Comprehensive Studies in Mathematics, Springer-Verlag, New York, 1986, p. 154.

[6]Finn, R., and Neel, R. W., "C-Singular Solutions of the Capillary Problem," *Journal für die Reine und Angewandte Mathematik*, Vol. 512, June 1999, pp. 1–25.

[7]de Lazzer, A., Langbein, D., Dreyer, M., and Rath, H., "Mean Curvature of Liquid Surfaces in Cylindrical Containers of Arbitrary Cross-Section," *Microgravity Science and Technology*, Vol. 9, No. 3, 1996, pp. 208–219.

[8]Weislogel, M., and Lichter, S., "Capillary Flow in an Interior Corner," *Journal of Fluid Mechanics*, Vol. 373, 1998, pp. 349–378.

[9]Weislogel, M., "Capillary Flow in Containers of Polygonal Section," *AIAA Journal*, Vol. 39, No. 12, 2001, pp. 2320–2326.

[10]Brakke, K. A., "The Surface Evolver," *Experimental Mathematics*, Vol. 1, No. 2, 1992, pp. 141–165; URL: http://www.susqu.edu/brakke/ [cited 15 Feb. 2006].

[11]Collicott, S. H., and Weislogel, M. M., "Computing Existence and Stability of Capillary Surfaces Using Surface Evolver," *AIAA Journal*, Vol. 42, No. 2, 2004, pp. 289–295.

[12]Chen, Y., Bacich, M., Nardin, C., Sitorus, A., and Weislogel, M., "The Shape and Stability of Wall-Bound and Wall-Edge-Bound Drops and Bubbles," *Microgravity Science and Technology* (to be published).

[13]Chen, Y., "A Study of Capillary Flow in a Vane-Wall Gap in Zero Gravity," Ph.D. Dissertation, School of Aeronautics and Astronautics, Purdue Univ., West Lafayette, IN, Aug. 2003.

[14]Chen, Y., and Collicott, S. H., "A New Design of Drop Tower to Study Uncertainties in Zero-Gravity Fluid Mechanics," AIAA Paper 2001-0609, Jan. 2001.

[15]Chen, Y., and Collicott, S. H., "Experimental Study on the Capillary Flow in a Vane–Wall Gap Geometry," *AIAA Journal*, Vol. 43, No. 11, 2005, pp. 2395–2403.

[16]Dussan, E. B. V, "On the Spreading of Liquids on Solid Surfaces: Static and Dynamic Contact Lines," *Annual Review of Fluid Mechanics*, Vol. 11, 1979, pp. 371–400.

S. Aggarwal
Associate Editor